ISSN 8755-6839

SCIENCE OF **TSUNAMI HAZARDS**

Journal of Tsunami Society International

Volume 40 **Number 3** **2021**

3D TOMOGRAPHY OF IONOSPHERIC ANOMALIES AFTER THE 2020 TURKEY EARTHQUAKE AND TSUNAMI USING GNSS-TEC

Mokhamad Nur Cahyadi[1,2*], Ira Mutiara Anjasmara[1], Ihsan Naufal Muafiry[3], Nurrohmat Widjajanti[4], Deasy Arisa[5], Buldan Muslim[6], Meilfan Eka Putra[1]

[1]Geomatics Engineering Department, Institut Teknologi Sepuluh Nopember, Indonesia
[2]Research Center of Science-Technology of Marine and Earth, Directorate of Research and Community Service, Sepuluh Nopember Institute of Technology, Surabaya, Indonesia
[3]Survey and Mapping Department, Politeknik Sinar Mas Berau Coal, Indonesia
[4]Geodetic Engineering, Universitas Gadjah Mada, Indonesia
[5]Research Center for Geotechnology, Indonesian Institute of Sciences, LIPI, Bandung, Indonesia
[6]National Institute of Aeronautics and Space, LAPAN, Bandung, Indonesia;
*email correspondence: cahyadi@geodesy.its.ac.id

ABSTRACT

Global Navigation Satellite System (GNSS) satellite observations can obtain Total Electron Content (TEC) values in the ionosphere layer. The TEC value is obtained by decreasing the phase difference of the GNSS satellite's two carrier waves (L-band). The calculation of the TEC value using GNSS can be used in disaster phenomena such as earthquakes observed in this study. The earthquake phenomenon can cause vertical deformation in the Earth's crust, resulting in the appearance of acoustic waves propagating towards the ionosphere layer and changes in the ionosphere density in a moment. A propagating gravity wave has a speed of 0.3 km/ s towards the ionosphere layer. This disturbed ionosphere layer was detected within minutes of the mainshock. The anomaly in this study was detected by Global Positioning System (GPS) Pseudo Random Noise (PRN) 16 from 16 observation GNSS stations on the mainland of Turkey. The observed ionosphere anomalies were then modeled

using tomography modelling to obtain spatial information from these anomalies. The tomography results found that the PRN 16 GPS satellites contained positive and negative anomalies located northeast of the epicenter.

Keywords: *3D Tomography, Earthquake, GNSS, Total Electron Content, Turkey Earthquake*

---

1. INTRODUCTION

The study of earthquake and tsunami disaster mitigation in geodesy and geomatics can be done by utilizing GNSS (Global Navigation Satellite System) system technology. This GNSS system is conducted to position a particular point on the Earth's surface accurately. GNSS is usually also used to monitor land subsidence (Anjasmara et al., 2018) and monitoring water vapor in the atmosphere (Cahyadi et al., 2018). Furthermore, GNSS satellite observations can be used to obtain TEC (Total Electron Content) values in the ionosphere layer. The TEC value obtained can be in the form of electron density along the line of sight (LoS) in the ionosphere layer called Slant TEC (STEC) or in the form of a vertical, which is commonly called Vertical TEC (VTEC). The use of GNSS satellites in obtaining TEC values is often used in observing ionospheric anomalies in earthquake phenomena (Cahyadi & Heki, 2015; Cahyadi & Heki, 2013a; Cahyadi & Heki, 2013b; Cahyadi, 2014; Cahyadi et al., 2018; Heki & Cahyadi, 2012; Sharma et al., 2017; Liu et al., 2011), tsunami (Kakinami et al., 2012; Muslim et al., 2020; Liu et al., 2006; Rolland et al., 2010), and volcanic eruptions (Shults et al., 2016; Nakashima et al., 2016; Cahyadi et al., 2020; Nakashima et al., 2014). Ionosphere disturbances can occur in several natural phenomena such as earthquakes, tsunamis, and volcanic eruptions. These phenomena can send acoustic waves propagating upward to the ionosphere layer, dominated by TEC (Cahyadi & Heki, 2015).

There was a strong earthquake (Mw 7) (USGS, 2020) from the east-west normal fault, which occurred on October 30, 2020 (11:51 UTC) between the offshore Seferihisar Izmir, Turkey, and the island of Samos, Greece. The focal mechanism shows a normal fault oriented in an east-west direction. The earthquake also caused a tsunami 11 minutes after the aftershock [Dogan et al., 2021] to reach a height of 6 meters and caused several coastal towns to be submerged as deep as 2 meters [Yalciner et al., 2020]. The aftershock earthquake happened about three hours later with 5 Mw magnitudes with a depth of about 15 km.

The vertical deformation resulting from the earthquake has caused the acoustic waves to move upward and sideways towards the ionosphere, disturbing electron density (Calais & Minster, 1995). Ionospheric disturbances observation using GNSS satellite have been carried out in the previous research (Cahyadi & Heki, 2015), which studied ionospheric disturbances caused by the 2012 North Sumatra earthquake with a magnitude of M 8.6. The quake was recorded as the largest strike-slip earthquake ever recorded and could destroy the oceanic lithosphere off the Indian Ocean coast of

North Sumatra. In this study, ionosphere anomalies were found 10-20 minutes after the earthquake occurred. Ionosphere disturbances were also observed in another research (Liu et al., 2011) which studied ionospheric disturbances caused by the 2011 Tohoku Japan earthquake with a magnitude of M 9. The quake generated vibrations on the Earth's surface which were very extraordinary and triggered a tsunami. Then the vertical deformation will produce disturbances in the ionosphere layer, which contains TEC assemblies. Ionosphere disturbances were recorded 7 minutes after the earthquake occurred with a velocity from the Earth's surface to the ionosphere layer of 833 m/s. Likewise, tsunami waves (even if only a few centimeters in the deep sea) can generate gravity waves which also move upward and sideways towards the ionosphere layer (Daniels, 1952). (Artru, 2005) observed the tsunami that occurred due to the Peru earthquake Mw = 8.2 in 2001 using GNSS network GEONET in Japan. The tsunami propagated towards the coast of Japan in the range of 20 to 22 hours after the aftershock. The amplitudes found in the traveling ionospheric disturbance show the magnitude of ±1 TECU.

Various observations were done to understand general characteristics of ionospheric disturbances, but imaging the ionospheric layer is still rarely obtained. Land-based 2D tomography modelling was done by Austen et al. (1988), which was then developed to observe traveling ionosphere disturbance (TIDs) by Pryse et al. (995), and Comberiate et al. (2007) used space-based UV tomography to describe plasma depletion at low latitudes. Kunistyn et al. (1997) also discussed the possibility of near-space environment tomography with GPS and ground-based stations. They showed that applying combinations of different satellite systems is beneficial in near-space environment tomography realization. Tomographic modelling was also used by Feng et al. (2021), who studied the phenomenon of the geomagnetic storm on June 17 and June 22, which occurred in Wuhan, China. This study used the TEC value to perform spatial analysis using tomographic modelling of the observed anomalies electron density changes. However, there is no detailed spatial information regarding the anomalies of the ionospheric layer in some of these studies, and it still uses STEC for tomography material.

The ionosphere observation method in this study was done using computerized tomography (CT). The usage of CT began in the previous survey (Austen et al., 1988), which introduced electron density depiction using CT modelling. The CT is beneficial to obtain spatial information on ionosphere disturbances detected in GNSS observations. This study will describe the ionosphere into a 3D tomographic model based on the altitude layer. Tomography 3D modelling requires observational data with different azimuths and elevations obtained from many stations around the earthquake area over a large area. The case of this study was the M 7 earthquake that occurred in Turkey on October 30, 2020. The result of this study is expected to plan an early warning system for the benefit of disaster mitigation.

The TEC value used in the study was obtained by differencing the phase difference of the carrier wave (L1 (~ 1.5 GHz) and L2 (~ 1.2 GHz)) from GNSS satellite observations. The TEC values obtained can be in the form of STEC and VTEC. STEC is the value of electron density contained along the LoS, while VTEC is the value of electron density that corresponds to the vertical direction of the ionosphere. The VTEC value is obtained by multiplying the cosine value of the zenith angle between the vertical direction and the direction of propagation of the GNSS satellite towards the Earth. The value of electron density is usually written as TECU (1TECU = 10^{16} electrons / m^2). The STEC value can be compared with the polynomial number line curve to obtain STEC residual. Significant difference values of TEC changes can be indicated as anomalous values for the ionosphere. The intersection between the ionosphere layer and the LoS is called the Ionospheric Pierce Point (IPP), while the projections on the Earth's surface are called the Sub-ionospheric Point (SIP).

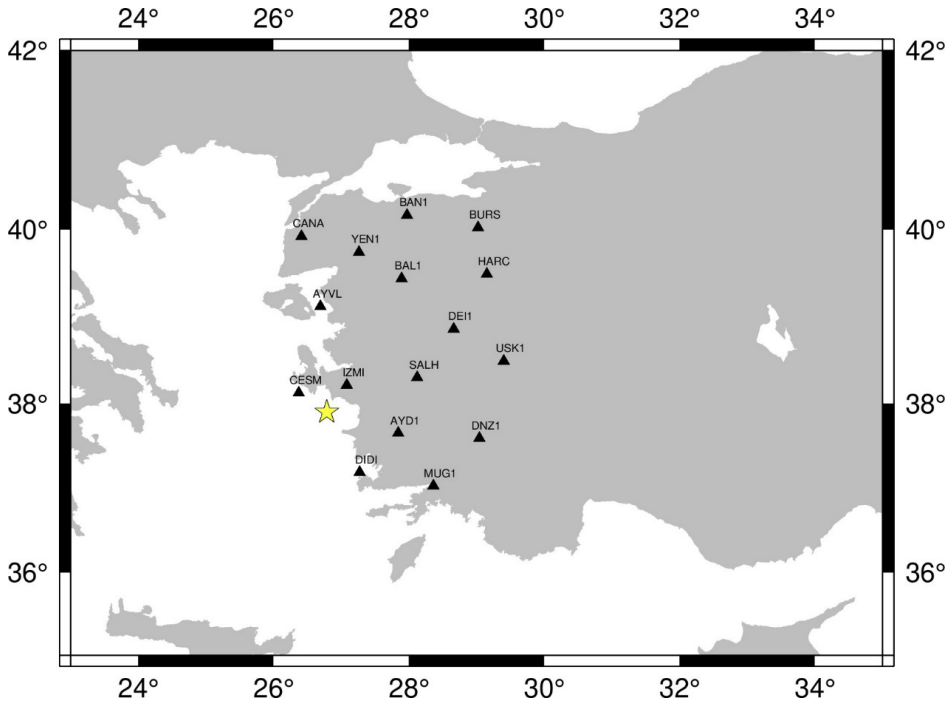

Figure 1. The distribution of GNSS observation stations and epicenter. The black triangle shows the location of GNSS stations, while the yellow star shows the epicenter location of the earthquake.

The tomography block was settled with the dimensions of 1° east-west direction, 1.2° north-south direction, and 75 km on the top-bottom side. Tomography blocks are assumed to be homogeneous. The division of ionosphere value for each LoS was done to get the electron density value in each tomography block based on the length of LoS penetration in a tomography block. The

length of LoS penetration is obtained from the length calculation of 2 LoS intersections with the sides of the tomography block. The value of density in the tomography block is obtained using the equation (He & Heki 2018):

$$\Delta \mathrm{STEC_i} = \sum_{j=1}^{n} A_{ij} x_j + e_i$$

This equation is used to obtain the density value of each tomography block passed by LoS using the LoS penetration length component in each block, the total TEC anomalous density value, and considering the measurement error value (it is assumed that 0.05 TECU originates from the typical error of differential GNSS measurements (Coster et al. 2013)).

3. RESULTS

3A. Ionosphere Anomaly Shortly After an Earthquake and Tsunami

The calculations were carried out using the equation of ionosphere linear combination to obtain TEC value on GNSS observations in the ionosphere layer along the observation path. The TEC value obtained will then be combined with the comparison value using a reference curve from the polynomial number with 6th order polynomial based on the best fitting line. Ionospheric anomalies can be detected at a STEC residual value which is significantly different from the reference curve. The anomaly value is obtained by calculating TEC changes and reducing the TEC value with the polynomial value of order 6. Anomaly changes in ionosphere density that experience disturbances were detected about 45 minutes after the mainshock or about 35 minutes after the tsunami on the PRN GPS satellite 16.

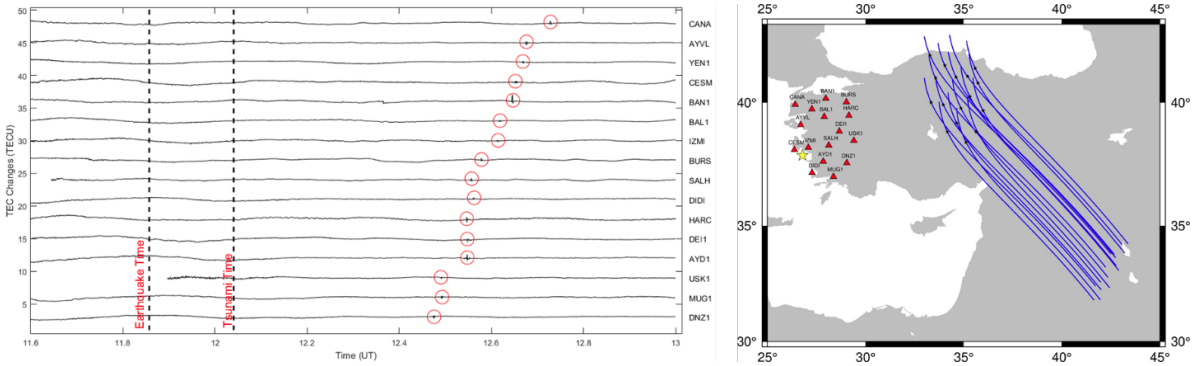

Figure 2. (Left) TEC time series from 2020 Turkey earthquake observed by PRN16 satellite. Two vertical lines indicate the time of earthquake and tsunami detected by USGS at 11.51 UT and 12.02UT, respectively. (Right) SIP trajectory at 11.00 – 14.00 UT, the small black star shows the time of the earthquake, the red triangle shows the observation station's location, and the yellow star shows the epicenter location.

Figure 2 shows ionosphere disturbances that occurred shortly after the mainshock repeatedly. The ionosphere anomaly was detected about 35 minutes after the tsunami, which was detected by 16 observation stations scattered around the epicenter. Then, GPS PRN 16 observed the gravity wave velocity at the tsunami traveling ionospheric disturbance (TTID) propagation of 0.3 km s-1. This propagation is consistent with the velocity of the gravity wave.

The deformation of Turkey's 2020 earthquake on October 30 at 11:51 UT is detected as strike-slip type. The Okada modelling calculation results based on the dip, strike and slip parameters obtained from the Global Centroid Moment Tensor (GCMT) are 246°, 67°, and -9 °. Figure 3 shows an uplift component for about 8 cm following the observation of Evelpidou et al. (2021). The vertical deformation of about 13 cm even mechanism of the earthquake is detected as strike-slip. Land subsidence was found more often compared to the uplift in this earthquake mechanism.

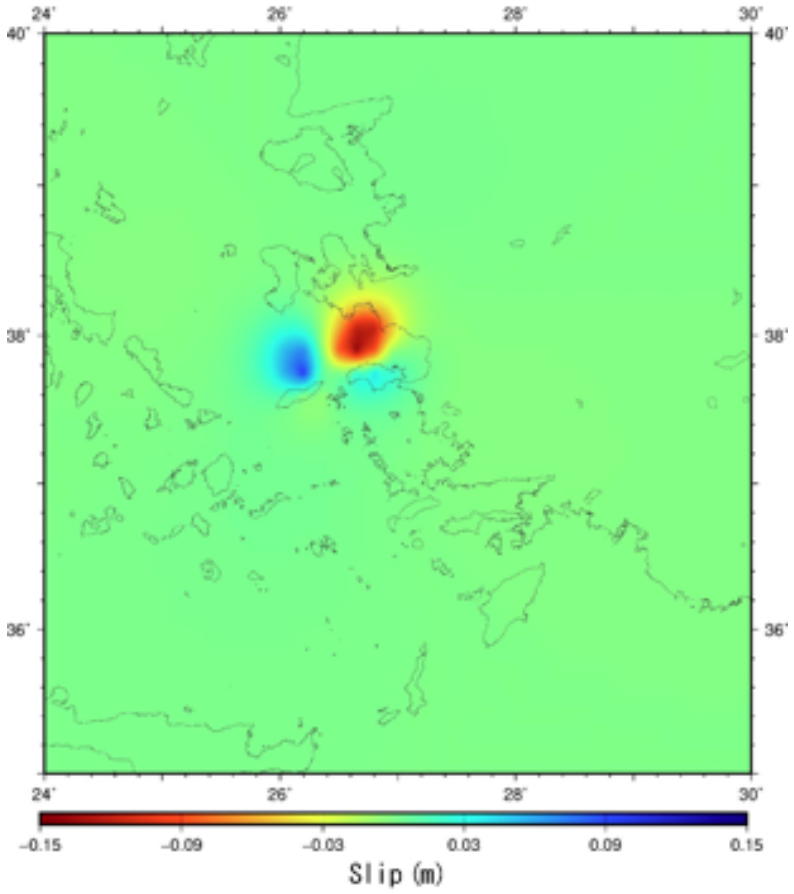

Figure 3. The vertical movement of the Earth's crust from 2020's Turkey earthquake. The earthquake was calculated using the Okada model (1992) and using fault geometry from GCMT.

3B. Tomographic model from Ionospheric Disturbance

The PRN 16 GPS satellites detected several ionospheric anomalies a few minutes after the earthquake. Anomalies were seen within 35 minutes after the tsunami. The anomaly was detected by 16 observation stations located around the epicenter of the quake.

The tomographic model (Figure 4) reports the density distribution of the ionospheric anomaly at each altitude at 100 Km intervals. In each tomographic model, the voxels containing the most anomalous payloads are at an altitude of 300 – 400 Km. In Figures 4(a-c), the positive anomaly appears at a lower altitude of about 200 km. In comparison, the negative anomaly appears in the east at a higher altitude, i.e., from 300 Km – 400 Km. Figure 4b is the tomographic model that has the largest value. It can be seen from the dense voxel color; this is because many stations detect anomalies at 32 minutes after the tsunami or 42 minutes after the earthquake.

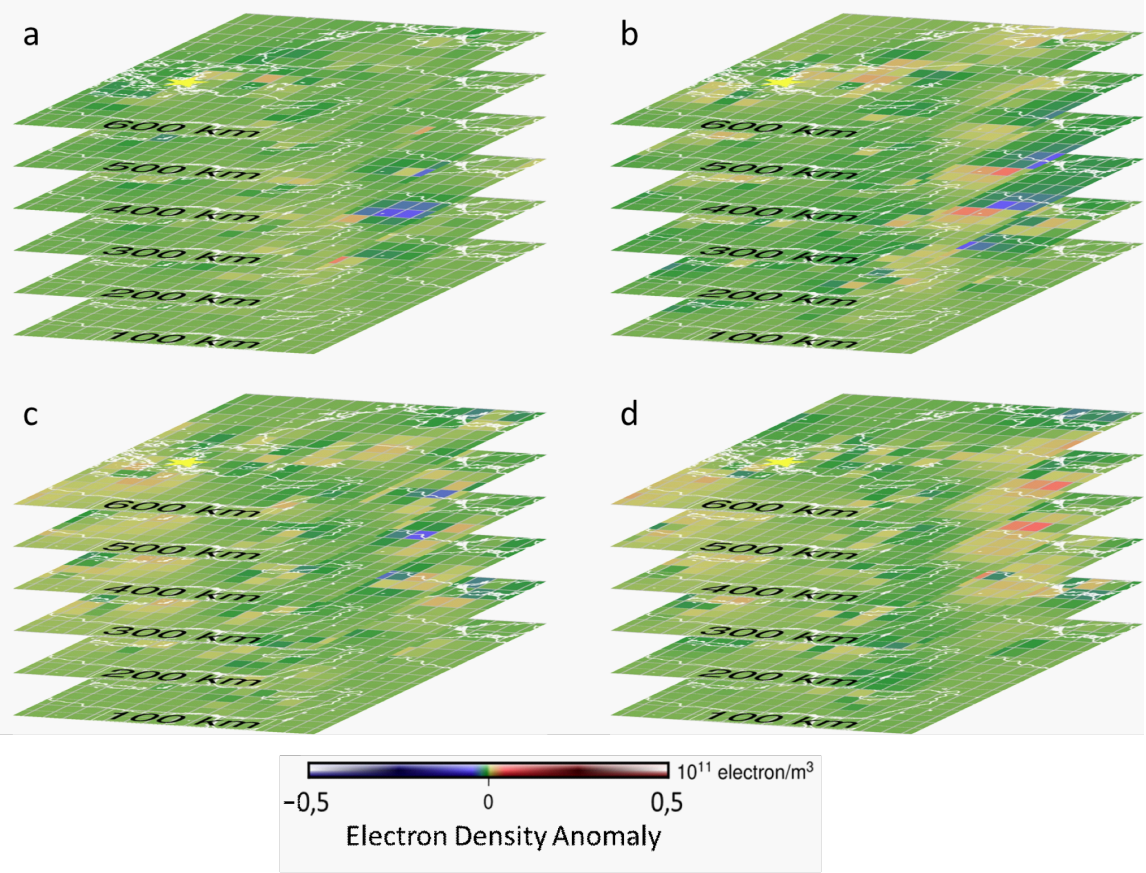

Figure 4. Tomographic model of (a) 29 minutes, (b) 32 minutes, (c) 40 minutes, and (d) 43 minutes after the tsunami. The small yellow star indicates the location of the epicenter, while the blue color tomographic voxel indicates a negative anomaly, while the red color indicates a positive anomaly.

3C. Accuracy Test

The checkerboard resolution test is used to analyze the reliability of electron density using a 3D tomography model. In this research, the investigation of ionospheric changes was conducted on the 2020 Turkish earthquake. STEC LoS anomaly data were synthesized, assuming a checkerboard-like distribution of electron density anomalies with 0.10 and –0.10 TECU/100 km.

Figure 5 (output) shows the anomaly distribution recovered from the synthesis model of checkerboard data. The picture shows that the 3D tomography finishes the high structure perfectly, as shown on the input image. By comparing both output displays, it can be concluded that the resolution on the higher altitudes (~200 km) is slightly worse than those with lower altitudes (~100 km). It is reflected by better coverage (more availability) of LoS for lower blocks. The output image shows that the resolution is higher over land and worse over the ocean.

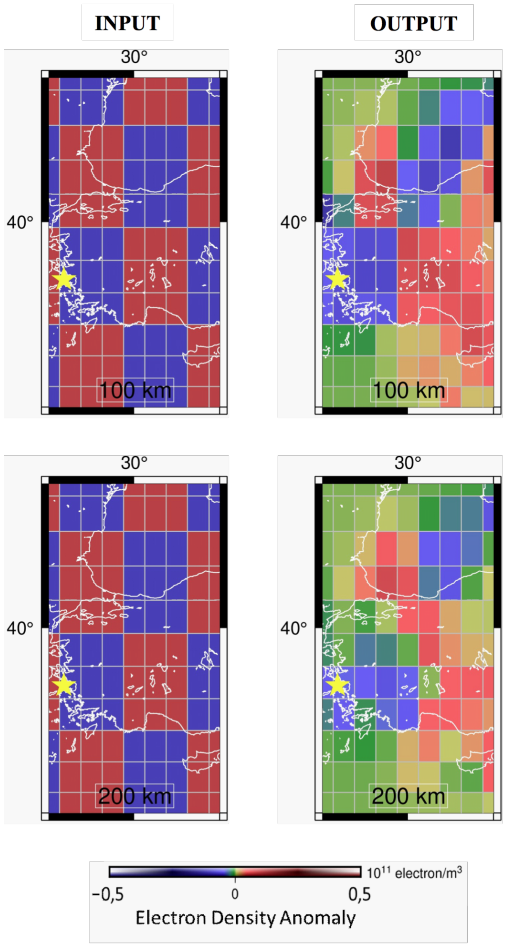

Figure 5. 3D anomaly pattern of electron density was used for checkerboard resolution with the height of 100 km (left) and 200 km (right). The alternating pattern of positive and negative anomalies was given at 0,15 and –0,15 TECU/100 km.

The comparison of STEC post-fit residual was conducted (Figure 6 on the lower panel) using STEC residual observation (Figure 6 on the top panel). The post-fit residue in each case shows much smaller dispersion, and the deviation standard is similar to the assumed error of STEC observation.

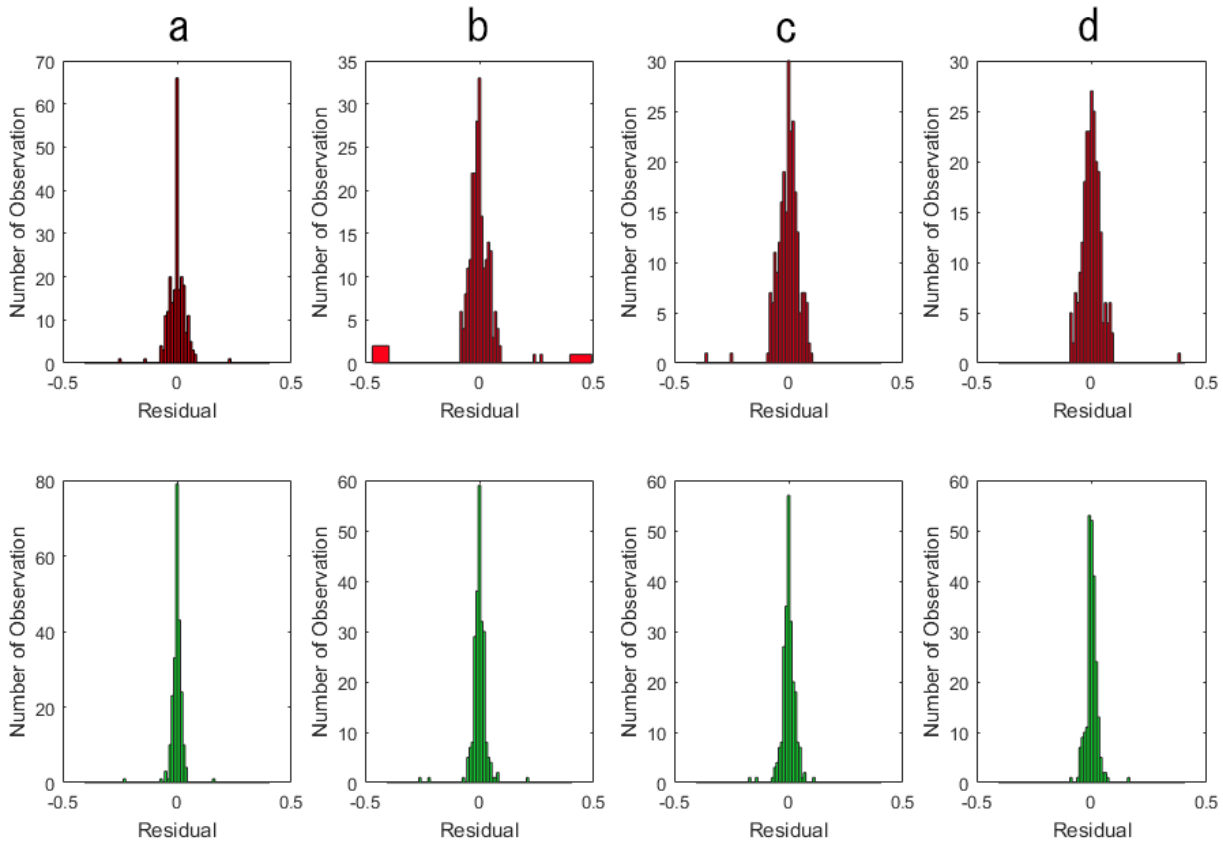

Figure 6. The input of STEC residual anomaly distribution (red) and the post-fit residual (x10^{11} electron/m^3) (green) for tomography model of (a) 29 minutes, (b) 32 minutes, (c) 40 minutes, and (d) 43 minutes after the tsunami. The post-fit residual becomes smaller than the observation, indicating that the tomography result has reproduced the observations adequately.

4. CONCLUSIONS

This study observed the 3D structure of the ionosphere's electron density anomaly immediately after the 2020 Turkey earthquake (Mw7.0) using GNSS-TEC data taken from mainland Turkey as the data input for the 3D tomography program. The appearance of ionosphere anomalies was detected by satellite GPS PRN 16 and happened about 45 minutes after the mainshock, around 35

minutes after the tsunami. It was found that the tsunami waves triggered atmospheric disturbances, which then propagated at an average speed of about 0.3 km/s into the ionosphere layer and significantly disrupted the electron density. This propagation speed is consistent with gravity waves and caused by tsunamis (Artru et al., 2005; Tsugawa et al., 2011; Cahyadi & Heki, 2015; Rolland et al., 2010; Savastano et al., 2017).

The visualization of ionospheric disturbances was done using tomography modelling to provide spatial information from the location of anomalies detected by GPS satellites PRN 16. Tomography offers information on the anomaly density of each voxel that has been arranged. The anomalies in this study were detected using PRN 16 GPS satellites were positive and negative anomalies located in the northeast of the epicenter. The usage of tomography can obtain spatial information from detected anomalies. The anomalies induced by gravity waves mainly distributed from 100 to 600 km in altitude, and their magnitude decreased with altitude. They showed similar orders of magnitude at the altitudes of 300 km and 400 km, and the magnitude decreased from 500 km with height. The performance of the tomography result was also confirmed using a resolution test, which is a checkerboard test. The result shows that the resolution at higher altitudes was slightly worse than at lower altitudes. The checkerboard test also indicates that the resolution is higher over land and worse over the ocean.

REFERENCES

Anjasmara, I. M., Yulyta, S. A., Cahyadi, M. N., Khomsin, Taufik, M., & Jaelani, L. M. (2018, July). Land subsidence analysis in Surabaya urban area using time series InSAR method. In AIP Conference Proceedings (Vol. 1987, No. 1, p. 020071). AIP Publishing LLC.

Artru, J., Ducic, V., Kanamori, H., Lognonné, P., & Murakami, M. (2005). Ionospheric detection of gravity waves induced by tsunamis. Geophysical Journal International, 160(3), 840-848.

Austen, J. R., Franke, S. J., & Liu, C. H. (1988). Ionospheric imaging using computerized tomography. Radio Science, 23(3), 299-307.

Cahyadi, M. N. (2014). Near-Field coseismic ionospheric disturbances of earthquakes in and around Indonesia. The Degree of Doctor of Philosophy. Dept. Natural History Sciences, Graduate School of Science, Hokkaido University.

Cahyadi, M. N., & Heki, K. (2013a). Ionospheric disturbances of the 2007 Bengkulu and the 2005 Nias earthquakes, Sumatra, observed with a regional GPS network. Journal of Geophysical Research: Space Physics, 118(4), 1777-1787.

Cahyadi, M., & Heki, K. (2013b). The Scaling Law of The Near-Field Coseismic Ionospheric Disturbances. In AGU Fall Meeting Abstracts (Vol. 2013, pp. NH13C-1625).

Cahyadi, M. N., & Heki, K. (2015). Coseismic ionospheric disturbance of the large strike-slip earthquakes in North Sumatra in 2012: M w dependence of the disturbance amplitudes. Geophysical journal international, 200(1), 116-129.

Cahyadi, M. N., Anjasmara, I. M., Khomsin, Yusfania, M., Sari, A., Saputra, F. A., ... & Rwabudandi, I. (2018, July). Coseismic ionospheric disturbances (CID) after West Sumatra earthquake 2016 using GNSS-TEC and possibility of early warning system during the event. In AIP Conference Proceedings (Vol. 1987, No. 1, p. 020019). AIP Publishing LLC.

Cahyadi, M. N., Audah, S., Mutia, N., & Aliyan, S. A. (2017, July). Analysis of weather changes in the region of Surabaya in 2015 and 2016 using water vapor data from GPS and terra MODIS satellite image. In AIP Conference Proceedings (Vol. 1857, No. 1, p. 080003). AIP Publishing LLC.

Cahyadi, M. N., Rahayu, R. W., Heki, K., & Nakashima, Y. (2020). Harmonic ionospheric oscillation by the 2010 eruption of the Merapi volcano, Indonesia, and the relevance of its amplitude to the mass eruption rate. Journal of Volcanology and Geothermal Research, 405, 107047.

Calais, E., & Minster, J. B. (1995). GPS detection of ionospheric perturbations following the 17 January 1994, Northridge earthquake. Geophysical Research Letters, 22(9), 1045-1048.

Comberiate, J. M., Kamalabadi, F., & Paxton, L. J. (2007). A tomographic model for ionospheric imaging with the Global Ultraviolet Imager. Radio Science, 42(02), 1-12.

Coster, A., Williams, J., Weatherwax, A., Rideout, W., & Herne, D. (2013). Accuracy of GPS total electron content: GPS receiver bias temperature dependence. Radio Science, 48(2), 190-196.

Daniels, F. B. (1952). Acoustical energy generated by the ocean waves. The Journal of the Acoustical Society of America, 24(1), 83-83.

Evelpidou, N., Karkani, A., & Kampolis, I. (2021). Relative sea level changes and morphotectonic implications triggered by the Samos earthquake of 30 October 2020. Journal of Marine Science and Engineering, 9(1), 40.

Feng, J., Zhou, Y., Zhou, Y., Gao, S., Zhou, C., Tang, Q., & Liu, Y. (2021). Ionospheric response to the 17 March and 22 June 2015 geomagnetic storms over Wuhan region using GNSS-based tomographic technique. Advances in Space Research, 67(1), 111-121.

He, L., & Heki, K. (2018). Three−dimensional tomography of ionospheric anomalies immediately before the 2015 Illapel earthquake, Central Chile. Journal of Geophysical Research: Space Physics, 123(5), 4015-4025.

Heki, K., & Cahyadi, M. N. (2012, December). Precursory changes in ionosphere immediately before mega-thrust earthquakes. In AGU Fall Meeting Abstracts (Vol. 2012, pp. NH43C-04).

Kakinami, Y., Kamogawa, M., Tanioka, Y., Watanabe, S., Gusman, A. R., Liu, J. Y., ... & Mogi, T. (2012). Tsunamigenic ionospheric hole. Geophysical Research Letters, 39(13).

Kunitsyn, V. E., Andreeva, E. S., & Razinkov, O. G. (1997). Possibilities of the near−space environment radio tomography. Radio Science, 32(5), 1953-1963.

Liu, J. Y., Chen, C. H., Lin, C. H., Tsai, H. F., Chen, C. H., & Kamogawa, M. (2011). Ionospheric disturbances triggered by the 11 March 2011 M9. 0 Tohoku earthquake. Journal of Geophysical Research: Space Physics, 116(A6).

Liu, J. Y., Tsai, Y. B., Ma, K. F., Chen, Y. I., Tsai, H. F., Lin, C. H., ... & Lee, C. P. (2006). Ionospheric GPS total electron content (TEC) disturbances triggered by the 26 December 2004 Indian Ocean tsunami. Journal of Geophysical Research: Space Physics, 111(A5).

Muslim, B., Cahyadi, M. N., Sunardi, B., & Kumalasari, C. J. (2020). THE SIMULATION STUDY OF GNSS SIGNAL REFLECTION IN MONITORING SEA LEVELS AND TSUNAMI. Science of Tsunami Hazards, 39(4).

Nakashima, Y., Heki, K., Takeo, A., Cahyadi, M. N., & Aditiya, A. (2014, December). Ionospheric disturbances by volcanic eruptions by GNSS-TEC: Comparison between Vulcanian and Plinian eruptions. In AGU Fall Meeting Abstracts (Vol. 2014, pp. NH33C-05).

Nakashima, Y., Heki, K., Takeo, A., Cahyadi, M. N., Aditiya, A., & Yoshizawa, K. (2016). Atmospheric resonant oscillations by the 2014 eruption of the Kelud volcano, Indonesia, observed with the ionospheric total electron contents and seismic signals. Earth and Planetary Science Letters, 434, 112-116.

Pryse, S. E., Mitchell, C. N., HEATON, J. T., & Kersley, L. (1995). Travelling ionospheric disturbances imaged by tomographic techniques. In Annales geophysicae (1988) (Vol. 13, No. 12, pp. 1325-1330).

Rolland, L. M., Occhipinti, G., Lognonné, P., & Loevenbruck, A. (2010). Ionospheric gravity waves detected offshore Hawaii after tsunamis. Geophysical Research Letters, 37(17).

Sharma, G., Mohanty, S., & Kannaujiya, S. (2017). Ionospheric TEC modelling for earthquakes precursors from GNSS data. Quaternary International, 462, 65-74.

Shults, K., Astafyeva, E., & Adourian, S. (2016). Ionospheric detection and localization of volcano eruptions on the example of the April 2015 Calbuco events. Journal of Geophysical Research: Space Physics, 121(10), 10-303.

Tsugawa, T., Saito, A., Otsuka, Y., Nishioka, M., Maruyama, T., Kato, H., Nagatsuma, T. & Murata, K.T., 2011. Ionospheric disturbances detected by GPS total electron content observation after the 2011 off-the-Pacific coast of Tohoku Earthquake, Earth Planets Space, 63, 875–879.

United States Geological Survey (USGS). 2020. M 7.0 - 13 km NNE of Néon Karlovásion, Greece. Accessed February 14, 2021, <https://earthquake.usgs.gov/earthquakes/eventpage/us7000c7y0/executive>

Yalciner, A. C., Dogan, G. G., Ulutas, E., Polat, O., Tarih, A., Yapa, E. R., & Yavuz, E. 2020. The October 30, 2020 (11:51 UTC) Izmir-Samos earthquake and tsunami: posttsunami field survey preliminary results.